

RADAR STUDIES OF AVIATION HAZARDS: Part 1

Storm Structure Algorithm

David J. Smalley
F. Ian Harris
Shu-Lin Tung
Alan R. Bohne

Hughes STX Corporation
c/o OL-AA PL/GPAB
29 Randolph Rd.
Hanscom AFB, MA 01731-3010

15 July 1996

DTIC QUALITY INSPECTED 2

Scientific Report No. 3

19970206 118

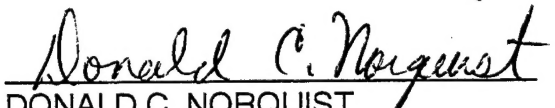
APPROVED FOR PUBLIC RELEASE; DISTRIBUTION UNLIMITED.



PHILLIPS LABORATORY
Directorate of Geophysics
AIR FORCE MATERIEL COMMAND
HANSCOM AIR FORCE BASE, MA 01731-3010

"This technical report has been reviewed and is approved for publication."


PAUL R. DESROCHERS
Contract Manager


DONALD C. NORQUIST
Acting Chief, Satellite Analysis and Weather
Prediction Branch
Atmospheric Sciences Division


DONALD A. CHISHOLM, Acting Director
Atmospheric Sciences Division

This report has been reviewed by the ESC Public Affairs Office (PA) and is releasable to the National Technical Information Service (NTIS).

Qualified requestors may obtain additional copies from the Defense Technical Information Center (DTIC). All others should apply to the National Technical Information Service (NTIS).

If your address has changed, or if you wish to be removed from the mailing list, or if the addressee is no longer employed by your organization, please notify PL/IM, 29 Randolph Road, Hanscom AFB, MA 01731-3010. This will assist us in maintaining a current mailing list.

Do not return copies of this report unless contractual obligations or notices on a specific document requires that it be returned.

REPORT DOCUMENTATION PAGE

Form Approved
OMB No. 0704-0188

Public reporting burden for this collection of information is estimated to average 1 hour per response, including the time for reviewing instructions, searching existing data sources, gathering and maintaining the data needed, and completing and reviewing the collection of information. Send comments regarding this burden estimate or any other aspect of this collection of information, including suggestions for reducing this burden, to Washington Headquarters Services, Directorate for Information Operations and Reports, 1215 Jefferson Davis Highway, Suite 1204, Arlington, VA 22202-4302, and to the Office of Management and Budget, Paperwork Reduction Project (0704-0188), Washington, DC 20503.

1. AGENCY USE ONLY (Leave blank)	2. REPORT DATE 15 July 1996	3. REPORT TYPE AND DATES COVERED Scientific No. 3		
4. TITLE AND SUBTITLE RADAR STUDIES OF AVIATION HAZARDS: Part 1. Storm Structure Algorithm		5. FUNDING NUMBERS F19628-93-C-0054 PE63707F PR 2781 TA GT WU MA		
6. AUTHOR(S) David J. Smalley, F. Ian Harris, Shu-Lin Tung, and Alan R. Bohne		8. PERFORMING ORGANIZATION REPORT NUMBER Hughes STX Scientific Report #8		
7. PERFORMING ORGANIZATION NAME(S) AND ADDRESS(ES) Hughes STX Corporation c/o OL-AA PL/GPAB 29 Randolph Road Hanscom AFB, MA 01731-3010		10. PERFORMING ORGANIZATION REPORT NUMBER PL-TR-96-2178(I)		
9. SPONSORING/MONITORING AGENCY NAME(S) AND ADDRESS(ES) Phillips Laboratory 29 Randolph Road Hanscom AFB, MA 01731-3010 Contract Manager: Paul R. Desrochers/GPAB		11. SUPPLEMENTARY NOTES		
12a. DISTRIBUTION/AVAILABILITY STATEMENT Approved for public release; distribution unlimited		12b. DISTRIBUTION CODE		
13. ABSTRACT (Maximum 200 words) Automated techniques have been developed to detect the three-dimensional structure of convective storms, with focus on the high reflectivity factor inner core to monitor the evolution of the Weak Echo Region, as a tool for the prediction of severe weather such as hail and tornadoes				
14. SUBJECT TERMS Doppler weather radar, automated techniques, supercells, storm structure, three-dimensional quantification		15. NUMBER OF PAGES 36		
17. SECURITY CLASSIFICATION Unclassified		18. SECURITY CLASSIFICATION OF THIS PAGE Unclassified	19. SECURITY CLASSIFICATION OF ABSTRACT Unclassified	20. LIMITATION OF ABSTRACT Unclassified

TABLE OF CONTENTS

1.0	INTRODUCTION	1
2.0	(B)WER STRUCTURE VARIABILITY	4
3.0	THE STORM STRUCTURE ALGORITHM	6
3.1	(B)WER Structure Identification	6
3.1.1	PREPROCESSING	8
3.1.1.1	Storm Cropping	8
3.1.1.2	Outlier Processing	8
3.1.2	FEATURE DETECTION	9
3.1.2.1	High Reflectivity Factor	9
3.1.2.2	Reflectivity Factor Gradient	11
3.1.2.3	High-Low-High Reflectivity Factor Patterns	13
3.1.2.4	(B)WER Feature Extraction	17
3.2	Precipitation Structure	19
4.0	CASE HISTORY	22
5.0	CONCLUSIONS	29
6.0	REFERENCES	30

1.0 INTRODUCTION

The interactions between the ambient environment, storm dynamics, and precipitation physics are complex but intrinsically deterministic of the types of thunderstorms which develop. These interactions generate the thunderstorms's precipitation and cloud structure which is monitored by Doppler radar. The severity of the resultant weather is directly related to the intensity of the thunderstorm. The most intense thunderstorms, supercells, account for a disproportionately high percentage of all thunderstorm-related severe weather events.

Byers and Braham (1949) documented the life cycle of the ordinary thunderstorm which begins with an updraft that initiates development of a cumulonimbus cloud. At maturity, the resultant precipitation falls through the generating updraft. This creates a downdraft that overwhelms the updraft in the final stage of the thunderstorm. This life cycle of a single updraft/downdraft thunderstorm cell typically occurs over an one hour period with little if any associated severe weather.

Most thunderstorms occurring in North America are not of a single cell nature but are multicellular (Burgess and Lemon, 1990). Convergence created from gust fronts, remnant outflow boundaries, and orographic influences can provide the focus for the production of a succession of single cells that merge or interact as a multicellular thunderstorm. With the proper combination of low-level moisture, instability, and wind shear, a single or multicellular thunderstorm evolves into a supercell having an unicellular character that appears quasi-steady-state over a period of a few hours. This steady-state appearance is because of the combined microphysical, dynamical, and environmental processes in the storm.

Knowledge of the internal structure of a supercell can provide the basis for a useful diagnostic tool. The first observations of the reflectivity factor structure of a supercell were made with conventional radar by Browning and Ludlam (1962). This supercell caused a severe hailstorm in Wokingham, England and was observed to have an echo-free vault beneath a high reflectivity factor core aloft. Donaldson (1962) described a similar vault structure as a chimney in an Oklahoma severe thunderstorm. In general, the vault area is likely to be of lesser reflectivity factor than its surroundings rather than literally echo free.

The two supercells were compared (Browning and Donaldson, 1963) and found to have a structure distinct from other thunderstorms. The authors surmised that this structure of supercells was indicative of an exceptionally powerful, persistent, and organized updraft. This vigorous updraft distinguishes supercells from ordinary thunderstorms and functions as its catalyst.

Chisholm (1973) observed that a number of hailstorms in Alberta, Canada also were of supercell structure. When a radar scans through the upper portions of the echo-free vault, a Plan Position Indicator (PPI) display will depict the vault as a ring of high reflectivity factor surrounding a "hole" of lower reflectivity factor. This "hole" was named the Bounded Weak Echo Region (BWER) by Chisholm. When viewed at lower levels, the PPI display will depict an open notch which is known as a Weak Echo Region (WER). For this paper, the combined three-dimensional feature will be referred to as a (B)WER. The reflectivity factor structure of supercells includes a number of key features:

- A (B)WER resulting from droplets being transported high into the storm by the updraft prior to reaching highly reflective sizes.
- The high reflectivity factor core capping the (B)WER is produced by drop growth and vertical convergence in a region of updraft deceleration.
- The shroud or "wall" of high reflectivity factor about the (B)WER delineating the descending precipitation outside the updraft core.
- A mid-level echo overhang resulting from interactions between the divergent flow above the maximum vertical velocity and the environmental wind.
- A hook or pendant-shaped echo located to the right rear of the low-level weak echo region.

With the advent of Doppler radar, it was deduced that many supercells have a cyclonically rotating vortex called a mesocyclone. Armstrong and Donaldson (1969) first discovered evidence of such a cyclonic vortex in a severe thunderstorm in Massachusetts.

Importantly, they noted that at times the mesocyclone was collocated with the updraft region inferred from the reflectivity factor structure. Donaldson (1970) presents criteria for vortex identification from Doppler radar radial velocity signatures. The mesocyclone typically forms at mid-levels of the supercell at or near the updraft location and, thus, likely near a (B)WER. The relationship of the mesocyclone to processes within the supercell as well as the occurrence of associated severe weather are extensively reported on in the literature and are beyond the scope of this paper.

The (B)WER is arguably the most distinct reflectivity factor structure associated with the updraft of supercells. It is not possible for a single scanning Doppler radar to measure updrafts. However, through temporal monitoring of pertinent reflectivity factor structures, an inference may be made about supercell strength and organization and the associated updraft. While the current suite of WSR-88D algorithms examine some aspects of the reflectivity factor structure, none are designed to automatically identify and quantify the (B)WER. Klazura and Imy (1993) note that the volume WER display is the only WSR-88D product to directly address the (B)WER. The display, with eight horizontal slices of reflectivity factor through the vertical extent of the storm, allows the operator visual detection capability but not automatic detection and quantification.

Hughes STX Corporation has developed a Storm Structure Algorithm to identify precursors to severe weather in the reflectivity factor field. This algorithm uniquely detects and quantifies the three-dimensional (B)WER within a supercell automatically and monitors it with time. In addition, the algorithm assesses the entire storm reflectivity factor structure in three dimensions. Thus, the evolution of the supercell and the (B)WER may be compared and related to the resultant severe weather.

The (B)WER structure and its variability are discussed in Section 2. The Storm Structure Algorithm is described in Section 3. A case study with results from the algorithm is detailed in Section 4. Results will be summarized in Section 5.

2.0 (B)WER STRUCTURE VARIABILITY

The BWER is bounded essentially because it has significantly extended into the mid-level overhang. Lemon (1977) notes that BWERs generally have a horizontal extent of no more than 8 km. The vertical extent of the BWER is about 3-5 km. The WER is generally larger than the BWER in horizontal extent. Thus, the three dimensional structure of the (B)WER indicates a WER at low levels that tapers towards a smaller, completely bounded BWER at mid-levels. In many cases, a WER may taper with height but never attain the BWER signature aloft.

As viewed in PPI format, the BWER is located in the highly reflective core region of the supercell marked by a perimeter ridge of high reflectivity factor enveloping a distinct minimum. Often, the ridge is observed to be comprised of the highest reflectivity factor in the supercell. Outside the ridge, there is a variable decrease in reflectivity factor. The WER, located at lower levels below the BWER, is similarly defined except that it is not bounded completely.

As described above, the BWER and WER are comprised of similar image signatures that are a response to microphysical and dynamical processes. The BWER appears donut-shaped in the PPI format. The WER appears as a reflectivity factor V-notch generally along the south-southeast flank of the supercell. Similar appearing notches that are not the WER are possible in a supercell's reflectivity factor signature. These extraneous notches present problems for (B)WER identification. Another problem is that the angle within the V-notch for WERs is quite variable and can even be obtuse.

(B)WER variability can also be considered as a function of supercell type. Supercells are typically described as classic, LP (low precipitation), and HP (high precipitation) types. Others (Bluestein and Parks, 1983) note that these descriptions may actually be stages of the overall supercell's evolution.

Each class of supercell has similar reflectivity factor field characteristics as those described previously. However, the relative positioning and/or size of these features within

the storm varies by type. Radar observations of LP supercells have shown them to be unicellular with small updraft regions. Bluestein and Woodall (1990) described LP supercells as skeletons of the classic supercell. LP supercells have been observed to yield a narrow swath of large hail. The relatively small sized updraft region of LP supercells makes (B)WER detection more difficult particularly at longer ranges because the WSR-88D data resolution for the reflectivity factor is 1 km in range, 1° in azimuth, and at least 1° in elevation angle separation.

Nelson (1987) notes that HP supercells have produced unusually long, wide, and destructive hail swaths but are less apt than classic supercells to yield strong or violent tornadoes. They are also associated with flash flooding and prolonged downburst events. HP supercells have been described as multicellular/supercellular in form. Observations indicate these supercells may have multiple (B)WERs or a large (B)WER fed by multiple updrafts. They have also been observed to transform rapidly to radar bow echoes.

HP supercells generally have a larger radar "footprint" than classic supercells. The WER is typically displaced to the east-central area of the low level echo (as opposed to the south-southeast location) with a broad right concave (kidney bean) shape. An S-shape reflectivity factor signature in PPI format can sometimes develop in the lower levels of the HP supercell. This is because entrainment of drier mid-level air from the west-northwest forms a rear inflow notch in close proximity to the WER.

The variability inherent to (B)WERs dictates that a detection algorithm be rooted in radar signatures responsive to the causative physical processes. These radar signatures are most pronounced in the reflectivity factor field as discussed previously. This variability precludes detection by means of positional or spatial considerations. Instead, the algorithm, to be discussed in the following section, builds towards the (B)WER detection by combining information about the various aspects of the reflectivity factor patterns related to the dynamics within the supercell.

3.0 THE STORM STRUCTURE ALGORITHM

The Storm Structure Algorithm is comprised of two major functional units: (B)WER Structure and Precipitation Structure. The following flow chart highlights the concepts used by the functional units.

Precipitation Structure

- Structure Characterization
 - Volume assessment
 - Layer assessment

(B)WER Structure Identification

- Preprocessing
 - Storm Cropping
 - Outlier Removal
- Feature Detection
 - High Reflectivity Factor
 - Reflectivity Factor Gradient
 - High-Low-High Reflectivity Factor Patterns
 - (B)WER Feature Extraction
- Structure Characterization
 - Volume assessment
 - Layer assessment
 - (B)WER Deficit assessment

3.1 (B)WER Structure Identification

The philosophy for the (B)WER structure identification is to utilize a methodology applicable to both the BWER and WER case. As noted previously, the (B)WER is comprised

of a perimeter ridge of high reflectivity factor encompassing a region of weaker reflectivity factor. The algorithm focuses on the detection of the (B)WER through identification of its perimeter ridge. The processing is confined to the supercell's core volume and is designed to account for the variability inherent to the (B)WER. Image analysis is used to isolate characteristics associated with the perimeter ridge. The image factors of importance are:

- high reflectivity factor,
- reflectivity factor gradient about the perimeter ridge, and
- a high-low-high reflectivity factor pattern across the (B)WER.

Additionally, a strategy for (B)WER identification through image analysis is adopted that is similar in concept to the MIT/Machine Intelligent Gust Front Algorithm (Delanoy and Troxel, 1993). After preprocessing, independent analyses of the reflectivity factor data are performed yielding multiple image characteristic interest arrays of the (B)WER feature. These characteristics are combined using weighting functions to cull the (B)WER image signature from the overall visual scene. This methodology differs from conventional processing which essentially builds an analysis on results from the previous processing step and consequently yields fewer independent products. The output from this detection process for each elevation plane is then analyzed for final (B)WER identification.

Computational load is reduced by processing the image data independent of spatial location coordinates. The coordinates are introduced for the physical computations performed in the structural characterization. Preprocessing and detection components of the (B)WER structure identification are applied sequentially to each elevation angle plane of the supercell volume. The results are combined to yield a three-dimensional (B)WER feature whose structure is characterized. Pertinent aspects of each of these components will be discussed in turn.

3.1.1 PREPROCESSING

Preprocessing involves limiting the (B)WER identification analysis to the high reflectivity factor core region of each supercell and utilization of a one pass filter for outlier replacement.

3.1.1.1 Storm Cropping

After isolating a supercell in the radar volume, the (B)WER identification is initiated by defining the core reflectivity factor region of a supercell. This core region is determined by finding the maximum range and azimuth bounds of a predefined reflectivity factor value applied to each elevation angle plane. The bounds that define the final core region volume are determined from the maximum and minimum extents of the set of individual elevation plane bounds. Typically, this results in a volume that, for each elevation angle plane, includes the high reflectivity factor core along with some of the weaker reflectivity factor region of the supercell surrounding the core. The storm cropping is intended to limit the processing volume to a maximum of about 1000 data points ($30^\circ \times 30 \text{ km}$) per elevation plane. The exact number is, of course, dependent on the spatial size of the core region and its proximity to the radar.

3.1.1.2 Outlier Processing

The (B)WER detection utilizes gradient information. Spurious data (outliers) may potentially degrade the usefulness of gradient data. Thus, outlier processing is applied to the core region reflectivity factor data. A 25 cell window (5 range gates by 5 radials) is applied across the data in each elevation plane. The mean and standard deviation are computed for each window. A cell is considered an outlier if its reflectivity factor falls outside the 2.5 standard deviation limit determined from its associated window. The reflectivity factor value of each outlier is replaced by its eight-neighbor mean. Figure 1 shows the summation weights applied to the eight-neighboring cells of a target cell outlier. Occasionally, a small standard deviation is computed in regions of weak gradient resulting in a few unnecessary

EIGHT NEIGHBOR FILTERING

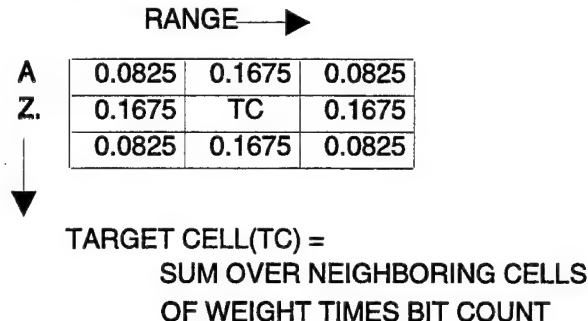


Figure 1. Weights for averaging filter for target cell.

substitutions. The impact of this is trivial compared to the benefit of actual outlier replacement.

3.1.2 FEATURE DETECTION

Feature detection processing involves performing three independent analyses of the preprocessed data to glean information from the image about the (B)WER perimeter ridge. Results of the perimeter detection are combined with information about weak reflectivity factor in the supercell core to yield extraction of the final (B)WER perimeter and interior.

3.1.2.1 High Reflectivity Factor

A simple model of a BWER was used to develop concepts for use in the (B)WER structure identification. Figure 2 shows the model BWER with reflectivity factor contours. Note the perimeter ring of highest reflectivity factor (white) in the center of the image array that envelops a minimum of reflectivity factor. The region of highest reflectivity factor within the core of the supercell is generally correlated with the (B)WER perimeter ridge location. To exploit this observation, a high reflectivity factor interest array is generated identifying the location of the top 20 percentile reflective cells within the image. Figure 3 shows the model BWER interest array for indication of the identified high reflectivity factor

region (white) along with the original contouring of reflectivity factor. Note that the model BWER perimeter ridge is completely included in this high reflectivity factor interest array.

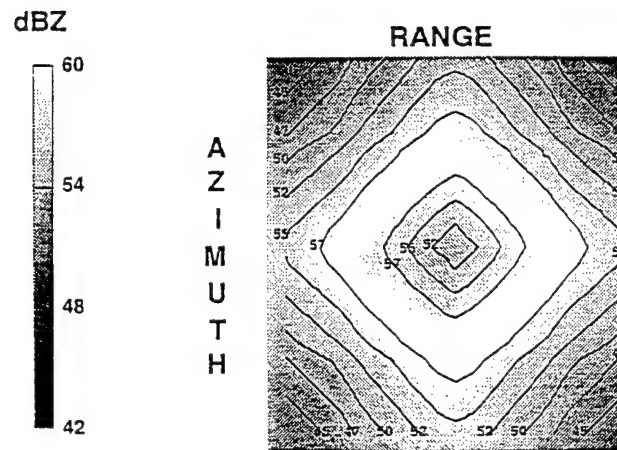


Figure 2. The model BWER image array with contours of reflectivity factor. The BWER is found in the center of the image and is comprised of the high reflectivity factor perimeter ring (white) and the lower reflectivity factor values within.

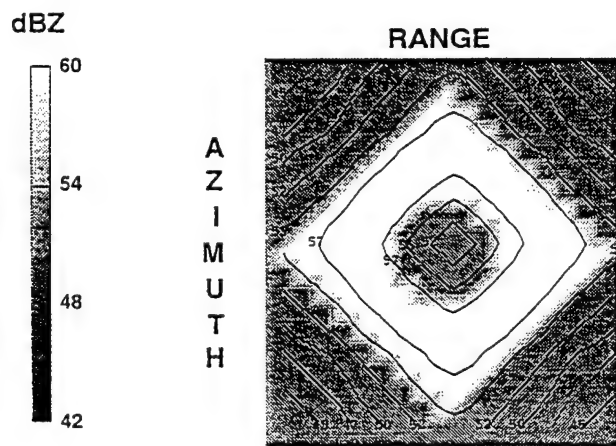


Figure 3. The high reflectivity factor interest array for the model BWER. The white region indicates the identified high reflectivity factor region of the image array. This region includes the BWER perimeter ridge.

3.1.2.2

Reflectivity Factor Gradient

Reflectivity factor gradient information has been found useful for detection of the (B)WER perimeter ridge. The (B)WER is assumed to be completely or partially surrounded by a ridge of high reflectivity factor. In a gradient field, this ridge should be apparent as a line or thin region of zero or near zero gradient across which the gradient changes sign. The linear gradient template shown in Figure 4 is used to compute the orthogonal gradient components across the unit interval image array. The components are combined to estimate the gradient direction and magnitude.

1	1	1
	TC	
-1	-1	-1

Δx

-1		1
-1	TC	1
-1		1

Δy

Figure 4. The orthogonal component templates of the gradient operator. TC is the target cell to which the component value is assigned.

For the model BWER of Figure 2, the lowest gradient magnitudes estimated using the orthogonal template are collocated with the perimeter ridge. In control cases, however, the natural variability of the reflectivity factor field generally results in at least 50% of the image having the same order of gradient magnitude as those found with the perimeter ridge. Currently, the use of gradient magnitude as a useful identifier has been discounted.

		RANGE km																			
		1	2	3	4	5	6	7	8	9	10	11	12	13	14	15	16	17	18	19	20
	300	0	0	0	0	0	0	0	0	0	1	1	1	1	1	1	1	1	1	1	1
	301	0	0	0	0	0	0	0	0	0	0	1	1	1	1	1	1	1	1	1	1
	302	0	0	0	0	0	0	0	0	0	0	1	1	1	1	1	1	1	1	1	1
	303	0	0	0	0	0	0	0	0	0	0	1	1	1	1	1	1	1	1	1	1
	304	0	0	0	0	0	0	0	0	0	0	1	1	1	1	1	1	1	1	1	1
	305	0	0	0	0	0	0	0	0	0	0	1	1	1	1	1	1	1	1	1	1
A	306	0	0	0	0	0	0	0	0	1	1	0	1	1	1	1	1	1	1	1	1
Z	307	0	0	0	0	0	0	1	1	1	0	0	0	1	1	1	1	1	1	1	1
I	308	0	0	0	0	0	0	0	1	1	1	1	0	0	0	1	1	1	1	1	1
M	309	0	0	0	0	0	0	1	1	1	1	1	0	0	0	1	1	1	1	1	1
U	310	0	0	0	0	0	1	1	1	1	1	0	0	0	0	0	1	1	1	1	1
T	311	0	0	0	0	1	1	1	1	0	0	0	0	0	0	1	1	1	1	1	1
H	312	0	0	0	0	0	0	1	1	1	0	0	0	0	1	1	1	1	1	1	1
deg	313	0	0	0	0	0	0	0	1	1	0	0	0	1	1	1	1	1	1	1	1
	314	0	0	0	0	0	0	0	0	1	0	0	0	1	1	1	1	1	1	1	1
	315	0	0	0	0	0	0	0	0	0	0	0	1	1	1	1	1	1	1	1	1
	316	0	0	0	0	0	0	0	0	0	1	1	1	1	1	1	1	1	1	1	1
	317	0	0	0	0	0	0	0	0	0	0	1	1	1	1	1	1	1	1	1	1
	318	0	0	0	0	0	0	0	0	0	0	1	1	1	1	1	1	1	1	1	1
	319	0	0	0	0	0	0	0	0	0	1	1	1	1	1	1	1	1	1	1	1
	320																				

0=NORTH COMPONENT

1=SOUTH COMPONENT

		RANGE km																			
		1	2	3	4	5	6	7	8	9	10	11	12	13	14	15	16	17	18	19	20
	300	1	1	1	1	1	1	1	1	1	1	1	1	1	1	1	1	1	1	1	1
	301	1	1	1	1	1	1	1	1	1	1	1	1	1	1	1	1	1	1	1	1
	302	1	1	1	1	1	1	1	1	1	1	1	1	1	1	1	1	1	1	1	1
	303	1	1	1	1	1	1	1	1	1	1	1	1	1	1	1	1	1	1	1	1
	304	1	1	1	1	1	1	1	1	1	1	1	1	1	1	1	1	1	1	1	1
	305	1	1	1	1	1	1	1	1	1	0	1	1	1	1	1	1	1	1	1	1
A	306	1	1	1	1	1	1	1	1	0	0	0	1	1	1	1	1	1	1	1	1
Z	307	1	1	1	1	1	1	1	0	0	0	0	0	0	1	1	1	1	1	1	1
I	308	1	1	1	1	1	0	0	0	0	0	0	0	0	0	1	1	1	1	1	1
M	309	1	1	1	1	0	0	0	0	0	0	0	0	0	0	1	1	1	1	1	1
U	310	0	0	0	0	1	1	1	1	0	0	0	0	0	0	0	0	1	1	1	1
T	311	0	0	0	0	0	1	1	1	1	1	1	1	1	1	0	0	0	0	0	0
H	312	0	0	0	0	0	0	1	1	1	1	1	1	1	0	0	0	0	0	0	0
deg	313	0	0	0	0	0	0	0	1	1	1	1	1	1	0	0	0	0	0	0	0
	314	0	0	0	0	0	0	0	0	1	1	1	0	0	0	0	0	0	0	0	0
	315	0	0	0	0	0	0	0	0	0	1	0	0	0	0	0	0	0	0	0	0
	316	0	0	0	0	0	0	0	0	0	0	0	0	0	0	0	0	0	0	0	0
	317	0	0	0	0	0	0	0	0	0	0	0	0	0	0	0	0	0	0	0	0
	318	0	0	0	0	0	0	0	0	0	0	0	0	0	0	0	0	0	0	0	0
	319	0	0	0	0	0	0	0	0	0	0	0	0	0	0	0	0	0	0	0	0
	320																				

0=EAST COMPONENT

1=WEST COMPONENT

Figure 5. The binary North/South and East/West coding of the gradient direction for the model BWER. The boxed cells reference the BWER ridge. Note that portions of the ridge lie along the transitions in the coded data.

Conversely, gradient directions have been found useful for identification of the (B)WER perimeter ridge. As noted, the BWER perimeter is expected to be in a region where the gradient direction changes sign. This sign transition is found by classifying each image cell's gradient direction into its orthogonal north-south and east-west components. Figure 5 illustrates this classification scheme with the model BWER. The boxed cells represent the high reflectivity factor perimeter ridge that defines the outer boundary of the model BWER. Notice that the perimeter is located along the orthogonal component transition in both the north-south and east-west analyses.

The gradient calculations across the `image` array assume a unit interval spatial separation in both processing directions. This expedites processing and eliminates the need for the associated spherical coordinates used for true spatial computations. For comparison purposes, gradient direction was computed using the associated spherical coordinates and classified as explained above. It was found that the identified transition zones were qualitatively similar and, thus, justifies use of the simple linear operators to minimize computational load.

3.1.2.3 High-Low-High Reflectivity Factor Patterns

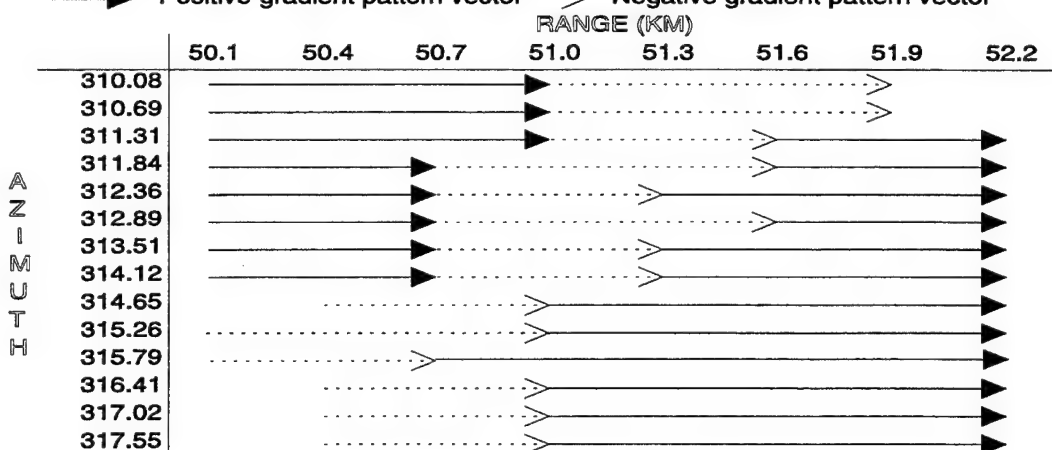
Pattern vectors (PV) for reflectivity factor are constructed in both cross-range (along a given radial) and cross-azimuth (along a constant range gate) directions of the image. A positive PV is defined as a vector where the reflectivity factor gradients are positive or zero. A negative PV is similarly defined except that the gradients are negative. At least three adjacent cells are required for a PV. This implies a minimum 3 km or 3° domain. While this operation is performed on the image unit interval array, it should be noted that the physical distances for cross-azimuth PVs increase with range from the radar.

		Sample Reflectivity Bit Count							
		RANGE (KM)							
		50.1	50.4	50.7	51.0	51.3	51.6	51.9	52.2
A Z I M U T H	310.08	169	177	181	195	190	180	173	180
	310.69	177	190	196	211	202	184	179	181
	311.31	192	198	211	218	202	185	189	189
	311.84	203	208	224	216	193	191	196	200
	312.36	204	218	231	213	194	195	204	210
	312.89	206	224	227	210	202	201	217	229
	313.51	210	220	225	210	204	212	232	244
	314.12	211	219	221	212	206	220	241	256
	314.65	214	221	219	209	213	229	248	263
	315.26	219	218	217	215	220	236	252	260
	315.79	223	218	216	222	224	235	251	257
	316.41	227	228	225	218	224	237	252	257
	317.02	231	237	225	222	225	245	257	265
	317.55	233	241	234	225	229	248	254	275

(a)

Cross range pattern vectors created from sample data

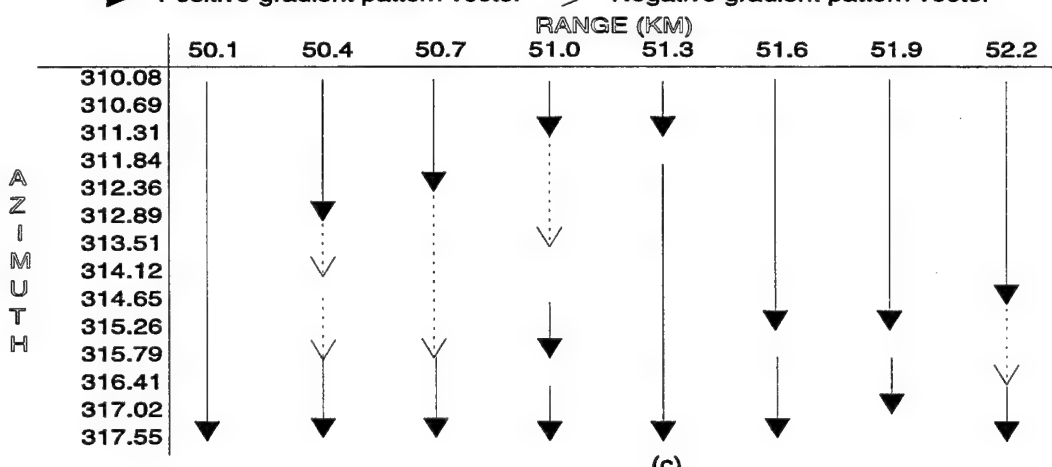
→ Positive gradient pattern vector → Negative gradient pattern vector



(b)

Cross azimuth pattern vectors created from sample data

→ Positive gradient pattern vector → Negative gradient pattern vector



(c)

Figure 6. A sample B-scan of the bit count reflectivity factor data are shown in (a). Cross-range (b) and cross-azimuth (c) pattern vectors based on this B-scan are also indicated. See text for discussion of pattern vectors.

Figure 6(a-c) is provided to illustrate the PV concept. Figure 6a shows a section from the control case with radar reflectivity factor in bit count. Only the relative values of the reflectivity factor are of concern here. Figures 6b and 6c depict the cross-range and cross-azimuth, respectively, positive and negative PVs associated with Figure 6a.

Any cell which is a juncture between PVs of opposite sign is an extremum; that is, a local maximum or minimum of reflectivity factor. Spatially, an extremum represents a local maximum or minimum over at least 5 adjacent cells (5 km or 5°). In Figure 7, extrema are identified as "1" for the model BWER case. Notice that the entire BWER perimeter ridge deduced from a manual analysis (boxed cells) is identified by extrema. Additionally, two orthogonal axes that cross at the BWER minimum are identified by extrema.

From a pattern recognition perspective, it is trivial to extract the BWER perimeter ridge for the simple model from extrema patterns. However, in nature, the pattern of PV-generated extrema is more convoluted. Often, the BWER perimeter ridge is not completely defined. The orthogonal axes, too, may not be contiguous and are likely to be at acute angles. Importantly, extrema unrelated to the ridge and axes may mask the basic (B)WER extrema pattern.

While the exclusive use of extrema for (B)WER perimeter ridge identification is not warranted with actual cases, extrema information is useful for identifying high-low-high (HLH) reflectivity factor patterns. With the analysis focused on the core region within the supercell, the juxtaposition of high to low to high reflectivity factor is a useful signature associated with the (B)WER. The definition of high reflectivity factor for HLH purposes relies on the interest array from the high reflectivity factor analysis.

Two definitions were explored for low reflectivity factor information: one based on magnitude, the other based on extrema. With low reflectivity factor defined as the lowest 20 percentile of magnitude, it was found that this region of low reflectivity factor often was not enveloped by the (B)WER perimeter but was on the outer edges of the image field. This means the low reflectivity factor inside the (B)WER perimeter ridge is greater than areas of low reflectivity factor outside the ridge. With this low reflectivity factor definition, the

analysis for HLH patterns results in a null case HLH interest array (i.e.- no feature is identified). This definition of low reflectivity factor will permit detection of (B)WERs with very low reflectivity factor inside the perimeter. Analyses to date indicate a greater likelihood of null cases resulting with use of this definition.

The identification of HLH patterns using the lowest percentile in magnitude sometimes results in the null case because of the storm cropping logic discussed previously. In some cases, a fast moving supercell may exaggerate the tilt of the core region. This can lead to an overabundance of low reflectivity factor especially at low and high elevation angles. This has the potential to compromise the HLH pattern processing because the lowest reflectivity factor is outside the ridge of high reflectivity factor. A solution to this would be to run a second pass of the cropping threshold on the individual image planes prior to further analysis.

The other, and seemingly superior, definition for low reflectivity factor is to use the PV-generated extrema associated with local minima. In this case, the lower reflectivity factor expected to be bounded by the high reflectivity factor (B)WER perimeter is relativistic (i.e.- a local minimum, not a percentile-based minimum). The resultant HLH interest array,

		RANGE km																				
		1	2	3	4	5	6	7	8	9	10	11	12	13	14	15	16	17	18	19	20	21
	303	1	
	304	1	
	305	1	1	1	
A	306	1	.	1	.	1	
Z	307	1	.	.	1	.	.	1	
I	308	1	.	.	.	1	.	.	.	1	
M	309	1	1	1	
U	310	1	1	1	1	1	1	1	1	1	1	1	1	1	1	1	1	1	1	1	1	
T	311	1	.	.	.	1	1	
H	312	1	.	.	1	1	
	313	1	.	.	1	.	.	1	
deg	314	1	.	1	.	1	
	315	1	1	1	
	316	1	
	317	1	

Figure 7. Model BWER extrema. Cells denoted "1" are extrema. The boxed cells reference the BWER ridge position. Refer to the text for more details.

independent of using either low reflectivity factor definition, indicates locations of high reflectivity factor cells that envelop low-defined reflectivity factor cells.

3.1.2.4 (B)WER Feature Extraction

The model BWER perimeter ridge is succinctly described independently by the high reflectivity factor, gradient direction, or HLH interest array or from a distinct extrema pattern. As discussed previously, none of these are suitable for independent detection of the (B)WER perimeter as found in nature. Combined, however, these interest arrays increase detectability of the (B)WER perimeter. A combined interest (CI) array is created through weighted summation of the individual interest arrays. Full weights are applied to both the high reflectivity factor and HLH interest arrays with quarter weights assigned to each of the orthogonal gradient direction interest arrays in the summation.

The CI array provides information about the (B)WER perimeter ridge but no information about the inner weak reflectivity factor region. Thus, the CI array is combined with the local minima information and HLH type logic is reapplied to detect the (B)WER perimeter and inner region for each elevation plane. These are combined to yield the three-dimensional volume of the (B)WER. This information is analyzed through Structure Characterization to yield two- and three-dimensional quantification estimates.

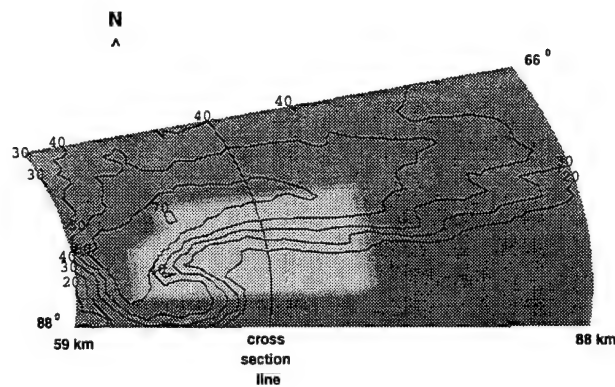


Figure 8. The Storm Structure Algorithm detected WER for the 0.5° elevation angle scan sector from Goodland, KS at 2028 UTC on May 12, 1995. The light shaded area indicates the position of the WER. Contours are in 10 dBZ increments of reflectivity factor. The cross section line is included for reference to Figure 11. See text for more detail.

Three examples are presented of the results of the (B)WER structure identification. All three are from an HP supercell monitored by the Goodland, KS WSR-88D on May 12, 1995 at 2027 UTC.

Figure 8 shows the detected WER in the 0.5° elevation angle plane (light shading) within the supercell core (dark shading). The figure also includes reflectivity factor contouring. Note that the WER is collocated with the V-notch in the contours. Also note the sharp gradient in the contouring with the WER as well as the 70 dBZ core on the northwest corner.

Figure 9 shows the detected BWER for this supercell at the 4.3° elevation angle plane. Note that the areal extent is much reduced compared to the WER of Figure 8. Notice that the BWER is comprised of a perimeter of about 60 dBZ enveloping an area of 50 dBZ. Also note the large area of lower reflectivity factor in the image located well away from the BWER. This is an example of where the local minima technique has clear advantage over the magnitude technique in defining the low reflectivity factor criteria for the HLH processing.

Figure 10 shows the three-dimensional (B)WER perimeter surface overlaying the reflectivity factor contouring for the lowest elevation angle plane (same as Figure 8). In this view, the broad low-level WER rapidly tapers to the BWER aloft. The centroid associated with the (B)WER is about 75 km from the radar at 83° with the least reflective region about 2 km aloft in the WER portion. A total volume of 839 km^3 is estimated.

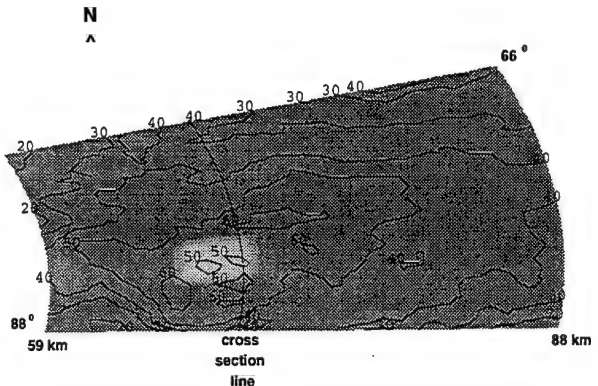


Figure 9. The Storm Structure Algorithm detected BWER for the 4.3° elevation angle scan sector from Goodland, KS at 2028 UTC on May 12, 1995. The light shaded area indicates the position of the BWER. Contours are in 10 dBZ increments of reflectivity factor. The cross section line is included for reference to Figure 11. See text for more detail.

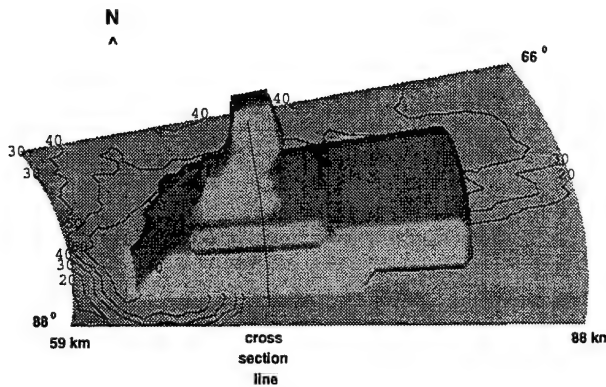


Figure 10. The Storm Structure Algorithm detected three-dimensional (B)WER for the scan sector from Goodland, KS at 2028 UTC on May 12, 1995. This is a composite from all the elevation angle scans in the storm volume including those presented in Figures 8 and 9. The contours for the 0.5° elevation angle scan are included for positional reference. The cross section line is for reference to Figure 11. See text for more detail.

(B)WER. This core inner region is likely near the axis of strongest upward vertical motion associated with the updraft. A further discussion of this volume and the entire (B)WER sequence of this supercell is presented in Section 4.

3.2 Precipitation Structure

The precipitation structure of the entire storm volume is characterized to complement and enhance the analysis of the (B)WER. The physical characteristics of the three-dimensional (B)WER volume are obtained through the same Structure Characterization used for the entire supercell volume. Both volumetric and areal (layer) characterization is performed. Mass-weighted centroids are computed for both. For the (B)WER, an inverse mass-weighted approach is adopted to focus centroid locations to the weakest (least reflective) area of the (B)WER. This biases results towards the WER which typically are observed to have lesser reflectivity factor than the BWER. Many time-height products are also derived

Figure 11 is of the same three-dimensional (B)WER cut away in the middle to view its vertical structure via contours of reflectivity factor. The (B)WER surface is light on the outside and dark on the inside with this cut away presentation. The contours are for the vertical plane at the cut away range. Two observations are noted. One, the outer (B)WER surface has two 60+ dBZ regions associated with its perimeter. One along the left side at mid-levels where tapering begins and the other towards the lower right. Two, the reflectivity factor contours along the vertical cut away plane clearly show an axis of lower reflectivity factor reaching towards higher altitude in the central core of the

that allow for temporal monitoring of the (B)WER and the total supercell volume.

The volume and areal layer assessment discussed above is applied to both the (B)WER and the entire supercell volume. A third aspect of structure characterization applicable to the (B)WER only is the concept of deficit analysis. That is, the difference in reflectivity factor inside and at the perimeter of the (B)WER. The magnitude of the former is likely to be strongly correlated to the dynamics of the updraft. The magnitude of the latter is resultant from a complex interaction of dynamical processes at various spatial scales and microphysical processes. A variety of methods are under examination to determine their utility.

An elementary approach is to determine a difference between reflectivity factor inside the (B)WER and around its defining perimeter. This approach is seen to be more complex when consideration is given to determining what values of reflectivity factor should be used. Typical candidates would be peak, mean, or some sort of weighted-mean values. Additionally, by changing units from dBZ, the deficit can be enhanced. For example, a 10 dB difference will be much larger if recomputed after conversion from the log scale using a 50 dBZ perimeter rather than a 40 dBZ perimeter.

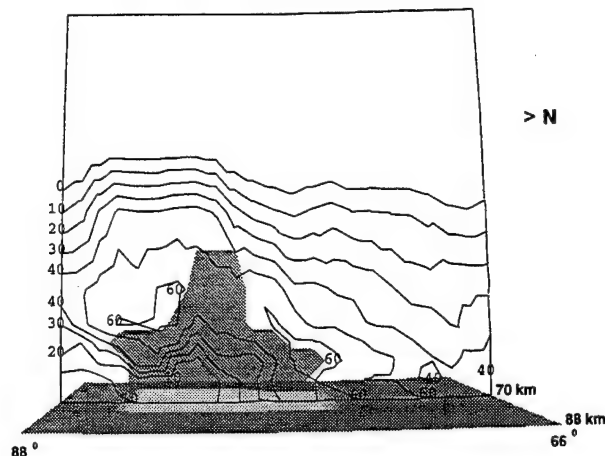


Figure 11. A cross section at 70 km through the Storm Structure Algorithm detected three-dimensional (B)WER for the scan sector of Figure 10. The reflectivity factor contours for the cross section are in 10 dBZ increments. Note the 60 dBZ contours located about the perimeter of the (B)WER. Also note the vertical extension of the lesser contours into the core of the (B)WER. See text for more detail.

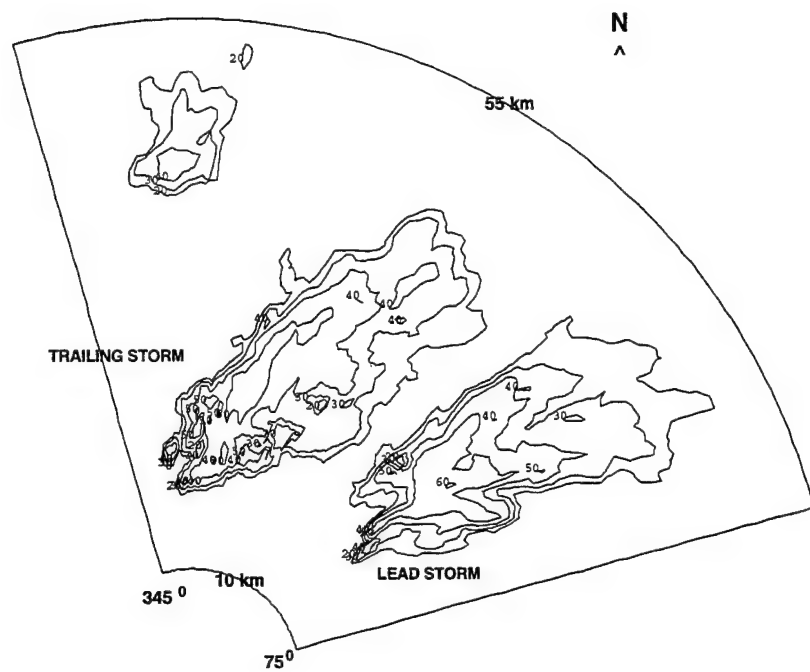


Figure 12. Reflectivity factor contours in 10 dBZ increments for 1904 UTC May 12, 1995 for Goodland, KS for the 2.4° elevation angle scan. At this time, the lead and trailing storms are distinctly separated. Refer to the text for further discussion.

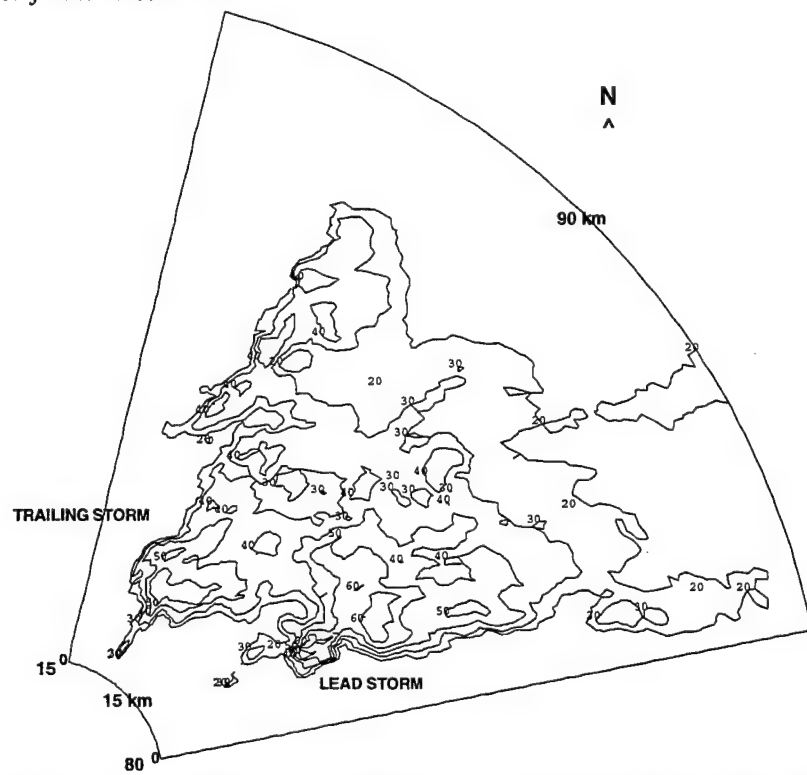


Figure 13. Reflectivity factor contours in 10 dBZ increments for 1940 UTC May 12, 1995 for Goodland, KS for the 2.4° elevation angle scan. At this time the trailing storm has caught the lead storm. Refer to the text for further discussion.

An alternative to the method discussed above is to monitor the height attained within the (B)WER of specific low reflectivity factor levels. This would be similar to the earlier method concerning the contours in Figure 11. The premise is that the greater height within the (B)WER attained by a low reflectivity value, the more severe the supercell.

4.0 CASE HISTORY

On May 12, 1995, an HP supercell located in northwest Kansas traveled almost due east slightly north of Interstate 70. This supercell was monitored by the Goodland, KS WSR-88D Doppler radar to the south. For much of its lifetime, it was within 100 km of the radar. This supercell was responsible for about \$4.5 million worth of damage with nearly \$1 million to non-crop property. The damage was caused by large hail, strong thunderstorm winds, and at least one F2 tornado (Storm Data, 1995).

The Storm Structure Algorithm was used to analyze this supercell on a whole storm basis and for the detection of any (B)WER. As would be expected with this type of severe storm, a (B)WER was automatically detected for about 100 consecutive minutes from 1940-2120 UTC. For about 53 consecutive minutes of that interval, a BWER was detected at mid-levels of the supercell as part of the overall detected three-dimensional (B)WER. This is the longest automatic detection and physical characterization of a (B)WER and BWER ever reported.

Radar observations of this supercell began with development in progress slightly northeast of the radar. Another storm was beginning to develop to the west. Over the next 50 minutes both storms matured and moved eastward. Figure 12 shows the relative positions

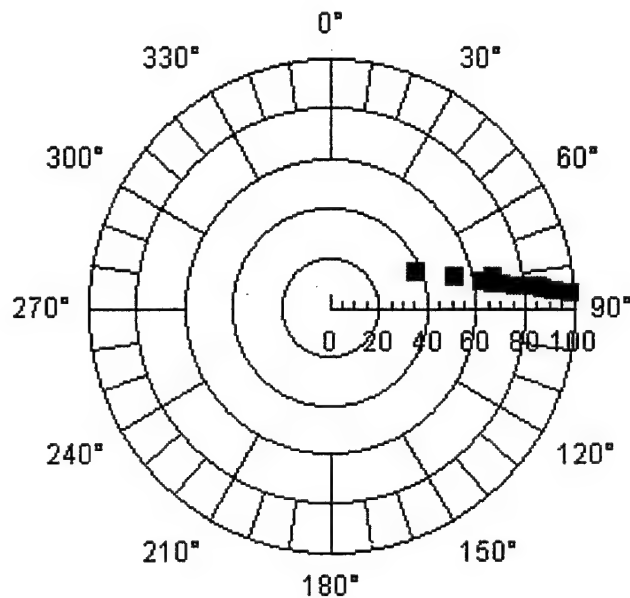


Figure 14. Position of detected BWER from the Goodland, KS WSR-88D radar from 1940 UTC (closest to radar) through 2103 UTC (farthest from radar).

of the two storms at 1904 UTC for the 2.4° elevation angle plane. Interestingly, the trailing west storm catches the lead supercell. They did not merge but maintained their separate identities appearing as abutting twin storms. Figure 13 shows their relative positions at 1940 UTC at the same elevation angle plane as Figure 12. They maintained this relationship over the next one and one half hours as the whole complex progressed eastward. All the while, the trailer storm slowly weakened in intensity.

About ten minutes before the two storms became abutted, the lead storm began to exhibit supercellular characteristics with sporadic development of a low-level WER. By 1940 UTC, the (B)WER had organized. In Figure 13, a small WER is observed open to the southeast. The WER is broad and flat with little curvature at low levels along the right front flank. This three-dimensional (B)WER is observed and detected for about 100 consecutive minutes beginning with the supercell volume of 1940 UTC. The first report of severe weather (2.5" diameter hail) from this supercell coincides with this time.

Also at this time, the mid-level BWER is first observed and detected. Like the earlier low-level WER, the BWER is sporadic in development initially but soon becomes well organized and long-lived. A total of fifteen BWER detections are made by the Storm Structure Algorithm for this supercell. From 2016-2109 UTC, the BWER at mid-levels is continuously detected as part of the overall three-dimensional (B)WER structure. The BWER is detected thirteen times in individual elevation angle planes in these nine supercell radar volumes. Thus, in some supercell radar volumes the BWER was detected at multiple elevation angle planes.

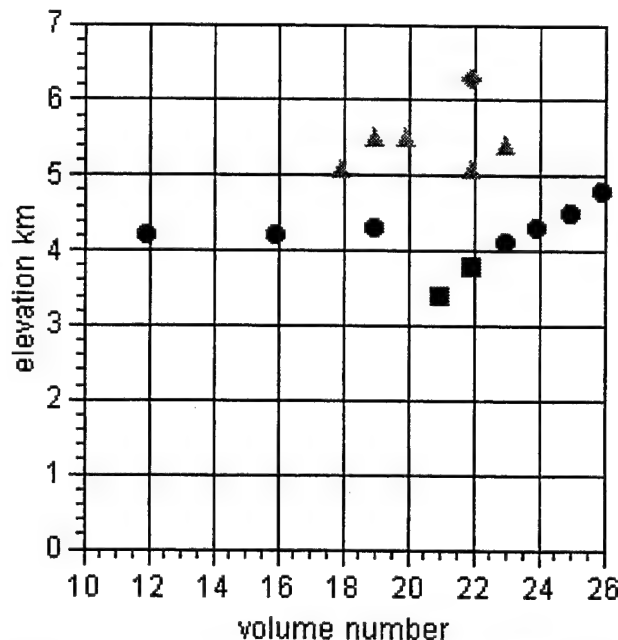


Figure 15. The elevation of the lowest reflectivity factor region of the detected BWERs in the supercell. The symbol shapes represent 1 km elevation ranges for cross-reference with Figure 16.

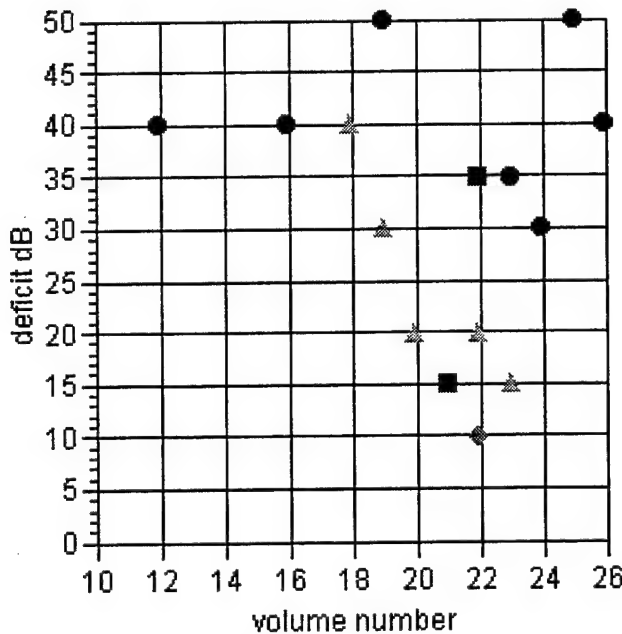


Figure 16. The deficit of reflectivity factor for each detected BWER. The symbol shape is for cross-reference to the elevation data of Figure 15. Squares are for the 3-4 km layer; circles are for the 4-5 km layer; triangles are for the 5-6 km layer; diamonds are for the 6-7 km layer.

the elevation that each BWER is detected at versus volume time of observation. The different symbols are used to indicate the 1.0 km interval to which the observation belongs. Recall that during this time interval the BWER moves from about 40 km to 100 km from the radar. The BWER is consistently located between about 4.0 - 5.5 km elevation despite the increasing distance of the supercell from the radar. Occasionally, the BWER is detected outside this elevation range.

Two factors influence the BWER detectability in this case. As the supercell moves further away, the lowest elevation that the BWER (and total (B)WER) can be detected increases. This is clearly seen in Figure 15 over the final half hour of detection. This is due to the range resolution issue inherent with radar. At distances greater than about 75 km from the radar, for this supercell, the BWER structure and vertical separation between the 1.5° and 2.4° beam axes is such that the lower beam passes below the BWER (detecting the WER) and the higher beam scans through the BWER increasingly higher above ground as the supercell moves away resulting in the impression of rising BWER elevation.

Figure 14 is a polar plot of the radial position of the lowest reflectivity factor area of the BWERs. The first BWER detection is 39 km from the radar while the last BWER detection is 100 km from the radar. The positions indicate the supercell traveled primarily east with a slow drift to the right. All along this path, there are reports of damage associated with the hail, thunderstorm winds, and tornadoes associated with this supercell.

During its period of detection, the BWER structure fluctuates in terms of altitude of detection, reflectivity factor deficit, and areal extent. Figure 15 charts

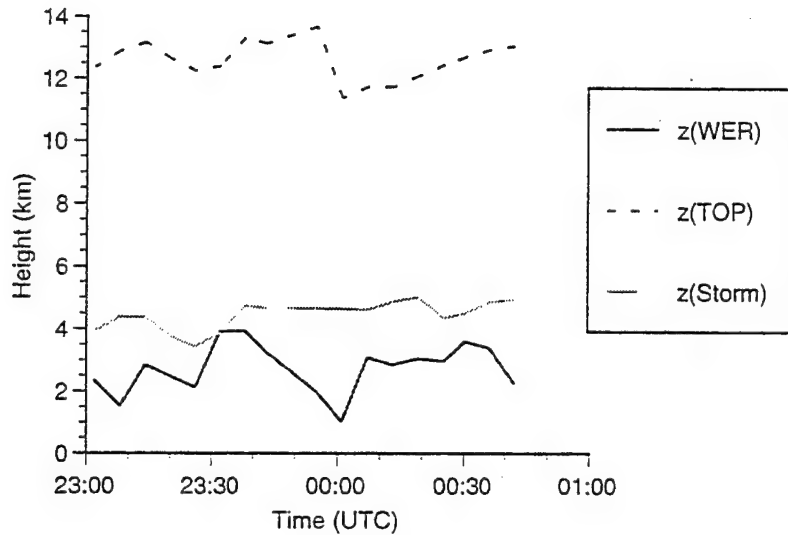


Figure 17. Height versus time plots of the (B)WER centroid, the storm centroid, and the storm top.

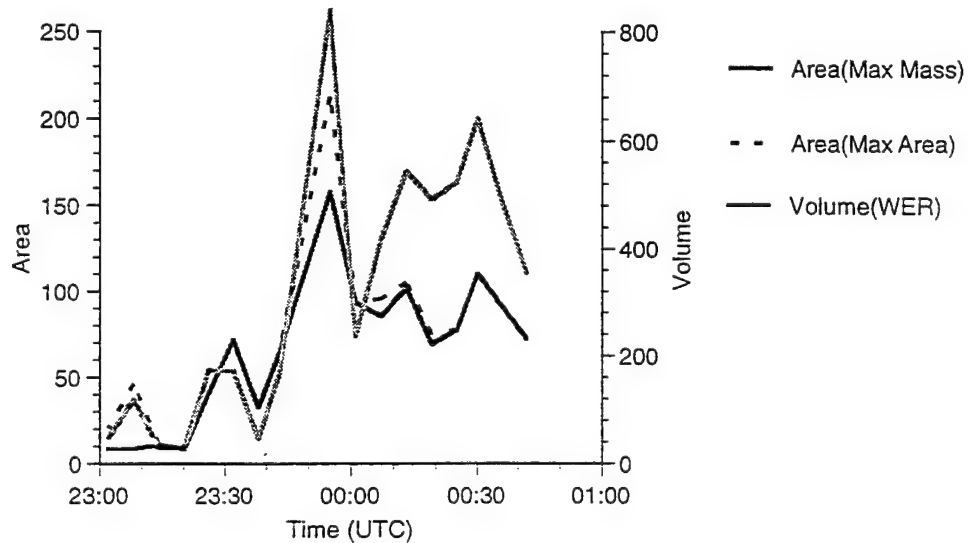


Figure 18. Time plots of WER volume and area layers where mass and areas are greatest.

Conversely, if the supercell were very close to the radar, the true upper reaches of the BWER may not be detected. Supercell dynamics strongly contribute to the BWER detectability. The distinct decrease in the detected BWER's elevation at volume 21 (2033 UTC) from earlier is a direct result of precipitation filling of the updraft region aloft. Note, also, that the BWER quickly reestablishes and is detected aloft immediately after the filling.

The collapse phase corresponds to the beginning of an 80 minute period in which intermittent F2 tornado damage was reported.

In Figure 15, a trend of establishment then collapse followed by re-establishment is observed for the BWER vertical profile. Figure 16 shows the reflectivity factor deficit estimate for each BWER detection versus time. The symbols in Figure 16 relate the deficit to the elevation corresponding to the same symbol for a given time in Figure 15. Deficit here is defined as the difference of approximate modal reflectivity factor values of the BWER interior from the BWER perimeter. The BWER perimeter modal values consistently were about 60 dBZ. Thus, the reflectivity factor deficit, and its fluctuations, is primarily responsive to the low reflectivity factor of the BWER interior which is responding to changes in the updraft character.

The deficit trend seen in Figure 16 is temporally similar to the trend observed with the elevation data. Further analysis shows that the deficit data depict a filling trend in the upper region of the BWER at least 12 minutes prior to evidence of such with the elevation data. Between 2016-2028 UTC (vol. 18-20), the BWER is observed above 5 km and indicates an increasing or steady height trend. The deficit data for the same interval, however, clearly shows the BWER at that level filling. Upon re-establishment of the BWER between 4.0 and 5.5 km, the deficit data show a steady increase towards the values prior to the filling episode.

The data in Figure 16 also clearly indicate that the core of the BWER (as defined by largest deficit) was consistently found between 4.0 - 4.5 km elevation. The portion of the BWER detected above this layer always had a lesser deficit that is indicative of the vertical proximity to the high reflectivity cap above the BWER. Application of this simple deficit definition adds to the qualitative assessment of temporal trends within the supercell. In this case, a more comprehensive temporal analysis is possible by combining the elevation and deficit trend information. Additional methods to account for the deficit concept such as discussed earlier will likely enhance the qualitative interpretation of trend analyses.

The structure characterization portion of the Storm Structure Algorithm is used to provide volume and areal estimates of the (B)WER and the entire supercell. This allows for

examination of the (B)WER in the context of the overall supercell. The data show that the supercell is actually quite vibrant with fluctuations of a somewhat cyclical nature and decidedly not steady-state.

Figure 17 is a time-height profile of a number of parameters for the identified (B)WER and supercell volumes from the structural characterization. The (B)WER centroid trace is of particular interest. It represents the mass-weighted height of the (B)WER center. The mass is derived from the reflectivity factor and the weighting is the inverse of the mass. This implies that the lower the reflectivity factor of a sample volume the greater its weighting influence for the centroid position. Since the largest area of weakest reflectivity factor is found at lower heights in the WER, this parameter is dominated by the WER and not the BWER region of the three-dimensional (B)WER.

Examination of the centroid trace shows a gradual height increase until about 2010 UTC. This is a direct indication of increasing height of lower reflectivity factor associated with the updraft and, in this case, coincides with the sporadic beginning of establishment of the BWER at mid-levels of the supercell as noted in Figure 15. The centroid height decreases until 2034 UTC and coincides with the filling aloft of the (B)WER as discussed earlier and illustrated in Figure 16 as reduced deficit. Lastly, the centroid height increases after this filling episode as the BWER is invigorated once again. The fluctuations in height of the (B)WER centroid is likely primarily driven by the WER areal extent of low reflectivity factor. The detection of the mid-level BWER and its height seem to have little influence on the centroid height fluctuations. The filling of the (B)WER from aloft was observed as a persistent trend of lowering centroid height. However, additional deficit information was necessary to distinguish that trend from other similar, but more minor, trends.

During the same time period, the supercell volume centroid was also computed. The greatest weighting for determining this centroid is directly proportional to the highest reflectivity factor values. As seen in Figure 17, it is much more consistent in height, generally between 4 and 5 km, than the (B)WER centroid. The supercell volume echo top height also shows fluctuations but is generally consistent in height. With the benefit of the

BWER deficit trend knowledge, it is interesting to note that a relatively sharp decrease in echo top height coincides with the climax of the filling episode. Early research of supercells identified the sudden decrease in echo top height as a potential indication of the onset of severe weather.

Figure 18 shows changes in the computed area and volume of the (B)WER. Two area representations are included. One is the value of the layer of greatest area of the (B)WER as found by the structure characterization. The other is the (B)WER area for the layer with the greatest “mass”. This “mass” is again based on the concept of maximum impact to the calculation from the lowest reflectivity factor values and focuses on the low-level WER. The fluctuations of all three parameters are in phase with each other.

The striking aspect of these curves is the pronounced maximum at 2028 UTC (vol. 20). This is the volume scan prior to the maximum filling of the (B)WER. It is seen in Figure 15 that the BWER at this time is found at about 5.5 km. The previous volume had a BWER detected at about 4.25 and 5.5 km. This implies that the WER was extended to a greater height at 2028 UTC. Thus, the tapering to the BWER from the WER in the vertical is reduced resulting in the greater volume. With decreasing height the WER opens to a larger area. A larger WER aloft implies a still larger WER below. The marked increase in area at this time occurs at a lower height (about 2.5 km) than the previous volume scan. In fact, the increasing trend in area (and volume) for the three volume scans ending at this peak occur at successively lower heights that are very near the (B)WER centroid heights at these times.

Thus, just prior to the beginning of reported F2 tornado damage from the supercell, a complicated situation is observed: a marked increase in areal and vertical extent of the WER occurs along with a BWER above that is steadily filling with precipitation. As noted previously, the filling of the (B)WER is maximized at 2034 UTC which is the volume scan immediately following this areal and volumetric peak. At that time, the WER volume and area sharply decrease. The BWER is now detected at about 3.5 km and has a very small deficit. The overall three-dimensional (B)WER is distinctly less robust in spatial and dynamical characteristics.

For this case study, the ability to detect and characterize the three-dimensional (B)WER within the overall supercell has led to new insight and intrigue about the development of severe weather. The various spatial and dynamical estimates that are now possible reveal in a unprecedented manner the changes within the core of this supercell. As more supercells are analyzed and possibly new characterization parameters are developed, a greater understanding and perspective will be developed as to the trends observed with this supercell.

5.0 CONCLUSIONS

The Storm Structure Algorithm (SSA) can identify and physically quantify the three-dimensional (B)WER within the high reflectivity factor core of supercells. The SSA as it is developed now appears to have improved detection capability for WERs from that reported on in previous annual reports because of an improved feature extraction technique. This results in a higher confidence in total three-dimensional (B)WER detection and assessment. With this detection it is now possible to monitor the physical characteristics of such and relate that to the occurrence of severe weather. Likewise, the SSA processes the entire supercell volume to generate a more inclusive Storm Structure assessment from the algorithm.

A case history was presented to illustrate the detection and monitoring of a three-dimensional (B)WER for about 100 consecutive minutes during a portion of a supercell's lifetime. Also, a mid-level BWER was observed as part of the overall three-dimensional structure for an unprecedented 53 consecutive minutes. During this time, large hail, strong thunderstorms winds, and a F2 tornado of long duration were reported (Storm Data, May 1995).

For the case study, structural characterization of the detected (B)WER was used to build a more complete description of the temporal changes within the supercell and the (B)WER. The areal and volumetric trends observed clearly show the non-steady-state nature of this supercell. While this case provides evidence for the utility of (B)WER detection and monitoring, sufficient evidence does not yet exist to suggest the prediction of severe weather

based on (B)WER precursors. A large database of supercells must be processed before formative results can be developed.

It is intended to develop the concept of (B)WER deficit further in future research. Particular emphasis will be placed on the idea of (B)WER and supercell core centroid juxtaposition and the height of weak reflectivity within the (B)WER. Additional tuning of the SSA (B)WER identification is anticipated as many more cases are analyzed.

6.0 REFERENCES

Armstrong, G. M., and R. J. Donaldson, Jr., 1969: Plan Shear Indicator for Real-Time Doppler Radar Identification of Hazardous Storm Winds. *J. Appl. Meteor.*, 8, 376-383.

Bluestein, H. B., and G. R. Woodall, 1990: Doppler-Radar Analysis of a Low-Precipitation Severe Storm. *Mon. Wea. Rev.*, 118, 1640-1664.

Bluestein, H. B., and C. R. Parks, 1983: A Synoptic and Photographic Climatology of Low-Precipitation Severe Thunderstorms in the Southern Plains. *Mon. Wea. Rev.*, 111, 2034-2046.

Browning, K. A., and F. H. Ludlam, 1962: Airflow in Convective Storms. *Quart. J. R. Meteor. Soc.*, 88, 75-84.

Browning, K. A., and R. J. Donaldson, Jr., 1963: Airflow and Structure of a Tornadic Storm. *J. Atmos. Sci.*, 20, 533-545.

Burgess, D. W., and L. R. Lemon, 1990: Severe Thunderstorm Detection by Radar. *Radar in Meteorology*, Atlas, D., ed., Amer. Meteor. Soc., Boston, MA, 619-647.

Byers, H. R., and R. R. Braham, Jr., 1949: *The Thunderstorm*. Supt. of Documents, U. S. Government Printing Office, Washington, D. C., 287 pp.

Chisholm, A. J., 1973: Alberta Hailstorms Part 1: Radar Case Studies and Airflow Models. *Meteor. Monogr.*, 14, Amer. Meteor. Soc., 1-36.

Delanoy, R. L., and S. W. Troxel, 1993: Machine Intelligent Gust Front Detection. Linc.

Lab. J., 6, 187-212, ESC-TR-93-346, ADA273481.

Donaldson, Jr., R. J., 1970: Vortex Signature Recognition by a Doppler Radar. *J. Appl. Meteor.*, 9, 661-670.

Donaldson, Jr., R. J., 1962: Radar Observations of a Tornado Thunderstorm in Vertical Section. NSSP Report No. 8, U. S. Weather Bureau, 1-21.

Klazura, G. E., and D. A. Imy, 1993: A Description of the Initial Set of Analysis Products Available from the NEXRAD WSR-88D System. *Bull. Amer. Meteor. Soc.*, 74, 1293-1311.

Lemon, L. R., 1977: New severe thunderstorm radar identification techniques and warning criteria: a preliminary report. NOAA Technical Memorandum NWS NSSFC-1, U. S. Dept. of Commerce, 60 pp.

Nelson, S. P., 1987: The Hybrid Multicell-Supercell Storm- An Efficient Hail Producer. *J. Atmos. Sci.*, 44, 2060-2073.

Storm Data, May 1995, NCDC, Asheville, NC.